Waves on unsteady currents

Merrick C. Haller
School of Civil and Construction Engineering, Oregon State University, Corvallis, Oregon 97330, USA

H. Tuba Özkan-Haller
College of Oceanic and Atmospheric Sciences, Oregon State University, Corvallis, Oregon 97330, USA

(Received 26 April 2007; accepted 2 October 2007; published online 3 December 2007; publisher error corrected 15 February 2008)

Models for surface gravity wave propagation in the presence of currents often assume the current field to be quasi-stationary, which implies that the absolute wave frequency is time invariant. However, in the presence of unsteady currents or time-varying water depth, linear wave theory predicts a time variation of the absolute wave frequency (and wavenumber). Herein, observations of wave frequency modulations from a large-scale laboratory experiment are presented. In this case, the modulations are caused by both unsteady depths and unsteady currents due to the presence of low-frequency standing waves. These new observations allow a unique and detailed verification of the theoretical predictions regarding variations in the absolute wave frequency. In addition, analytic solutions for the variations in frequency and wave height induced by the unsteady medium are found through a perturbation analysis. These solutions clarify the dependency of the wave frequency/wave height modulations on the characteristics of the unsteady medium. We also find that analytic solutions for simplified basin configurations provide an order of magnitude estimate of the expected frequency modulation effect. Finally, the importance of this phenomenon in natural situations is discussed. © *2007 American Institute of Physics*. [DOI: 10.1063/1.2803349]

I. INTRODUCTION

The influence of currents on waves and of waves on currents, i.e., wave-current interaction, can be significant in certain areas of the ocean. Some relevant studies illustrating the effects of wave-current interaction in coastal and nearshore areas have considered the changes in wavenumber and phase speed of waves as they propagate over a spatially varying but depth-uniform and steady current,[1] the change in surface wave heights due to tidal currents,[2,3] wave-current instabilities leading to the onset of rip current cells,[4] and the refraction of waves due to shallow water vortical motions.[5,6] For the case of depth-uniform currents, wave-current interaction theory is generally well developed and comprehensive reviews can be found in Refs. 7–13.

In practice, the vast majority of wave-current interaction analyses are done using the quasi-stationary current assumption, which considers the current field (and total water depths) to be stationary at time scales relevant to the wave propagation problem. In this case, the wavenumber of an incident monochromatic wave is affected spatially by wave-current interaction, but the wave frequency remains unaltered. However, there are a limited number of studies that consider unsteady currents and/or total water depth, for which linear water wave theory predicts modifications to the absolute wave frequency. The unsteady problem was first identified in the works of Unna,[14] Barber,[15] and Longuet-Higgins and Stewart.[7] Later, Irvine[16] discussed the problem in a purely numerical study, and Tolman[17] concluded through a model analysis that unsteadiness of currents and depths should be important to wave propagation in the North Sea. Özkan-Haller and Li[5] also noted the potential importance of the effect in the modeling of wave-driven longshore currents. However, direct model-data comparisons of modifications to the wave frequency have been sparse. Barber[15] observed a correlation between absolute frequency and the semidiurnal tide for a site off southwest Britain. Tolman[18] and Wolf and Prandle[19] presented limited data that showed some correlations between absolute period and tidal current velocity, but neither of these data sets contained the necessary observations to differentiate between the effects of unsteady currents and unsteady winds on the observed wave periods. Jones[20] presented observations from southwest Wales and concentrated on the refractive effects of strong tidal currents. They concluded that unsteadiness needs to be accounted for; however, direct model-data comparisons were not given. Consequently, to date the theory has not been validated with direct comparisons to observations, though unsteady current effects ought to occur in many natural situations, such as wave propagation through a tidal inlet or incident wave interactions with nearshore standing long waves (i.e., surf beat).

In the present work, we carry out direct comparisons of observed and predicted modulations to the absolute wave frequency due to unsteady currents and depth fluctuations. For this purpose, we analyze wave-current interaction in a large scale laboratory flume where the unsteady currents and the total water depth fluctuations are the result of the natural seiching modes of the tank. The lab experiments were not specifically designed to test wave-current interaction theory; however, it turns out that the experimental conditions are well-suited for analyzing modulations in wave kinematic properties induced by unsteady currents and water depths. It should be noted that the frequency modulations observed herein are fundamentally different from the "anomalous" dis-

persion previously reported for surf zone waves (see Elgar and Guza,[21] and references therein), which is time invariant and attributable to reflection of the incident waves at the shoreline.

Theoretical estimates of the expected wave frequency modulation in the presence of low-frequency motions are obtained using linear water wave theory. We summarize this basic theory and calculate the expected seiching modes in the laboratory tank in Sec. II. In Sec. III, we first demonstrate that the observed low-frequency motions correspond to the lowest mode seiche. Next, we show detailed comparisons of the predicted and observed frequency modulations due to wave-current interaction. In Sec. IV, we derive simplified analytic solutions regarding the effects of the currents on the wave kinematics in order to isolate the important aspects. These approximate solutions are shown to capture most of the behavior of the full linear solution. Section IV also includes a discussion of potential effects on nearshore wave heights. Finally, the conclusions are summarized in Sec. V.

II. THEORY

A. Linear wave theory for wave propagation in an unsteady medium

We consider a unidirectional monochromatic wave train propagating over a collinear current field, $U(x,t)$, which is assumed to be uniform in the vertical but spatially and temporally variable over scales (x,t) larger than those of the individual incident surface gravity waves. As a result, the kinematic properties of the surface waves propagating through this unsteady medium are altered. In particular, waves propagating over an opposing (following) current will shorten (lengthen). The current field is also allowed to have a surface signature $\eta(x,t)$, and there is an additional effect on the kinematics caused by the unsteady variations in the total water depth (comprised of the still water depth and the surface fluctuations due to the low-frequency field). In this work, $\eta(x,t)$ is considered to be slowly varying in space and time; hence, it does not contain the fluctuations due to the surface gravity waves. It can be interpreted as a wave-averaged surface elevation. Similarly, $U(x,t)$ does not contain the orbital velocities of the incident waves.

For waves propagating through the unsteady medium, spatial and temporal changes in the incident wave frequency are possible. These effects can be described by the linear dispersion relationship. The dispersion relation for the incident gravity waves propagating over an unsteady (but slowly varying) current U with associated surface elevation signal η is given by

$$(\omega - kU)^2 = gk \tanh kd, \tag{1}$$

where ω is the absolute frequency, k is the wavenumber, and g is the gravitational acceleration. The total water depth in which the waves are propagating is defined as $d=h+\eta$, where h is the still water depth.

For the inhomogenous and unsteady case where both d and U are allowed to vary in space and time, the time rate of change of the absolute wave frequency is found by differentiating Eq. (1) with respect to time and employing the conservation of wave crests principle (see, e.g., Ref. 22)

$$\frac{\partial k}{\partial t} = -\frac{\partial \omega}{\partial x}. \tag{2}$$

This gives the governing equation

$$\frac{\partial \omega}{\partial t} + (U + c_{gr})\frac{\partial \omega}{\partial x} = k\frac{\partial U}{\partial t} + q\frac{\partial \eta}{\partial t} - p\frac{\partial \eta}{\partial t}, \tag{3}$$

where c_{gr} is the relative group velocity, defined as the speed of wave energy propagation in a frame moving with the local current velocity. The quantities c_{gr}, q, and p are defined as

$$c_{\mathrm{gr}} = \frac{1}{2}\left(1 + \frac{2kd}{\sinh 2kd}\right)\frac{\omega - kU}{k}, \quad q = \frac{\omega k}{\sinh 2kd}, \tag{4}$$

and

$$p = \frac{k^2 U}{\sinh 2kd}.$$

These equations are essentially the same as those given in Mei[10] (p. 96) or Dingemans[23] (p. 55) and have been utilized by, among others, Tolman,[17] Özkan-Haller, and Li,[5] and Yu.[4]

Note that Eq. (3) is in the form of a forced advection equation and contains some implicit nonlinearity because c_{gr} is a function of the frequency ω. The right-hand side is explicitly dependent on the acceleration of the current and the surface elevation signal of the current. This indicates that temporal variations in the wave frequency only occur when the medium is unsteady, i.e., in the presence of accelerating currents and/or unsteady water depths. Finally, since the equation is of advection type, any anomaly in absolute wave frequency will propagate through the domain with velocity $U+c_{\mathrm{gr}}$. Hence, locally observed changes in frequency are not necessarily locally generated. This property was illustrated in the numerical simulations of Özkan-Haller and Li.[5]

B. Low frequency seiching modes

In a long enclosed flume there exists a family of natural seiching modes, which are standing shallow water waves of the form

$$\eta(x,t) = \hat{\eta}(x)e^{i\Omega t}, \quad \text{and } U(x,t) = \hat{u}(x)e^{i\Omega t}, \tag{5}$$

where Ω is the frequency and $\hat{\eta}(x)$ and $\hat{u}(x)$ describe the modal profile in the longitudinal direction (i.e., the long dimension of the flume). The frequencies and mode shapes can be obtained from the linearized shallow water equations and solutions for a number of basin geometries can be found in Wilson.[24] Typically, higher frequency modes are preferentially damped by friction and the lowest frequency mode is dominant in observations. The profile of $\hat{\eta}$ for the lowest mode has antinodes at the basin boundaries with a single node somewhere in the interior. The associated velocities are zero at the two ends of the flume with a maximum in the interior located at the surface elevation node.

Following the method of Kirby *et al.*,[25] the shallow water equations were solved numerically to obtain the seiching frequencies and mode shapes for the present bathymetry (see

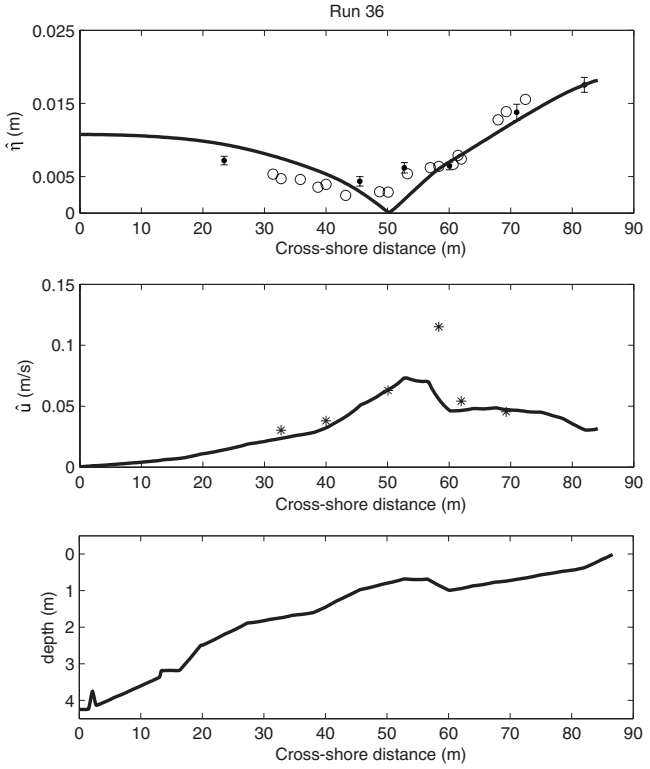

FIG. 1. (Top) cross-shore variation of $\hat{\eta}$, model (solid line) data (circles), error bars indicate variability for repeated measurements; (middle) cross-shore variation of $\hat{u}$, model (solid line) data (*); (bottom) fixed, barred beach bathymetry.

Fig. 1, bottom panel). From these results the frequency of the lowest seiching mode is calculated to be 0.0185 Hz. The associated mode profiles, $\hat{\eta}$ and $\hat{u}$, are shown as solid lines in Fig. 1 (top and middle panels). Note that the amplitudes of $\hat{\eta}$ and $\hat{u}$ obtained from this calculation can be arbitrarily scaled, because of the linearized nature of the governing equations.

III. COMPARISON TO OBSERVATIONS

The present observations of time variations in the absolute wave frequency were discovered by serendipity in the analysis of data from a large scale experiment designed for other purposes. The details of those original experiments can be found in Refs. 26 and 27. Here we summarize only the experimental details pertinent to the present analysis.

The experiments were performed in the large wave flume (LWF) at the O. H. Hinsdale Wave Research Laboratory (Oregon State University) in September 2004. The usable length of the LWF is approximately 90 m, and it is 3.7 m wide and 4.6 m deep. A flap-type wavemaker is located at one end of the flume and is equipped with active wave absorption capabilities, in order to reduce wave reflection. For the experiments discussed here, the bottom was configured into a piecewise continuous, barred profile, and the active wave absorption capabilities of the wavemaker were not utilized.

The LWF coordinate system has the x-axis pointing onshore along the centerline with the origin at the wavemaker, where the water depth was 4.27 m. Six resistance-type wave gages were used to measure free surface elevation and were sampled at 50 Hz. The wave gages were installed on a wall of the tank at cross-shore locations $x=23.5$, 45.4, 52.7, 60.0, 71.0, and 82.0 m and are referred to here as WG1 through WG6. In the present work, data from six regular wave conditions were analyzed and the relevant experimental parameters are listed in Table I. The equivalent deep water wave heights were calculated by deshoaling the wave heights measured at the offshore wave gage (WG1).

TABLE I. Experimental conditions for all runs: mean incident wave period T, equivalent deep water wave height H_o, relative water depth at the offshore gage $(kh)_1$, and relative seiching amplitude $(\hat{\eta}/h)_6$ at the most shoreward gage. Relative current scale $(\hat{u}/c_w)_{\max}$ is based on the cross-shore maximum of the ratio of the seiching current amplitude and the local incident wave phase speed.

Run	T (s)	H_o (m)	$(kh)_1$	$(\hat{\eta}/h)_6$	$\left(\frac{\hat{u}}{c_w}\right)_{\max}$
35	2.7	0.57	1.38	0.031	0.019
40	4.0	0.40	0.82	0.025	0.015
36	4.0	0.63	0.82	0.049	0.029
37	5.0	0.51	0.63	0.043	0.025
38	6.0	0.47	0.52	0.051	0.029
33	8.0	0.37	0.38	0.041	0.024

A. Observations and predictions of seiching

Analysis of the surface elevation time series clearly shows the presence of low-frequency waves. For example, the energy density spectrum calculated from the most shoreward gage (WG6) for run 36 is shown in Fig. 2 and the low-frequency portion shows a dominant peak at 0.0183 Hz (54.6 s). The seiching characteristics are expected to be similar for all of the tested wave conditions, indeed similar peaks exist at this frequency in all the wave gage records for all experimental runs. This is very near the predicted frequency of the lowest seiching mode (0.0185 Hz).

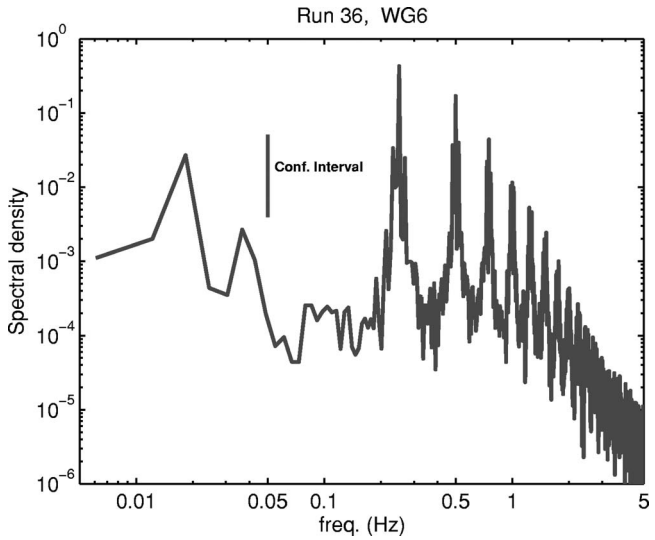

FIG. 2. Energy spectrum from WG6 run 36. Surface elevation time series were windowed and multiplied by a Kaiser window resulting in a frequency resolution of $\Delta f=0.006$ Hz and 6 dof.

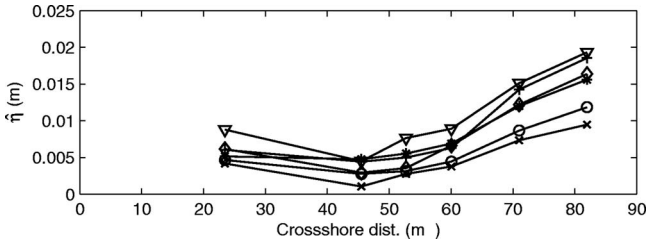

FIG. 3. Cross-shore variation of low-frequency amplitude, $\hat{\eta}(x)$, at $f=0.0183$ Hz; R35 (o), R40 (×), R36 (+), R37 (◇), R38 (△), R33 (*), 6 dof.

As mentioned previously, the modeled profiles $\hat{\eta}(x)$ and $\hat{u}(x)$ are shown in Fig. 1. Since the model amplitudes are of arbitrary magnitude, the profiles have been normalized so that they match the observed value of $\hat{\eta}$ (for $f=0.0183$ Hz) at WG6. From the measured water surface time series we estimate $\hat{\eta}$ using $\hat{\eta}=2|\hat{F}|$, where $\hat{F}$ is the spectrally averaged Fourier coefficient at a given wave gage and seiching frequency.

For the comparisons in Fig. 1 we used supplementary data previously collected by Scott *et al.*[28] on the same bathymetry in the LWF using a wave condition very similar to our run 36 ($T=4$ s, $H_0=0.57$ m). Since those authors achieved a much higher spatial resolution by repeated runs of the same wave condition and by using a mobile wave gage, this allows a more detailed comparison to the modeled mode profile. In addition, those authors also collected velocity time series at six cross-shore locations, which allows us to compare the modeled cross-shore velocity amplitudes, $\hat{u}$, to the observations.

The observations of $\hat{\eta}$ in the top panel of Fig. 1 show high amplitudes near the boundaries and indicate the existence of a nodal point near the center of the tank. However, observed amplitudes near the nodal point are nonzero. This is likely the result of both the existence of a small propagating component at this frequency and also the noise level of the *in situ* gages. Overall, the figure demonstrates good agreement between the theoretical seiching mode shape and the observed amplitudes. The middle panel of Fig. 1 compares the measured and calculated amplitudes of $\hat{u}$. These also compare very well except for one outlying point near $x=60$ m. Further investigation of the velocity data at that location showed an elevated noise level in that sensor during that experimental run.

The observed $\hat{\eta}$ for all of the experimental runs in the present data set are shown in Fig. 3 and likewise demonstrate that all runs show higher seiching amplitudes near the boundaries and a nodal point near the center of the tank ($x\approx 45$ m). The largest amplitudes overall are found close to the shoreline and the magnitude of these amplitudes vary between 1 cm and 2 cm. Larger seiching amplitudes are consistently observed for higher incident wave heights and longer incident periods. All of these profiles display a structure that is consistent with that expected of the lowest seiching mode.

Finally, as shown in Fig. 4, the cross-shore variation of the relative phase and coherence at the seiching frequency

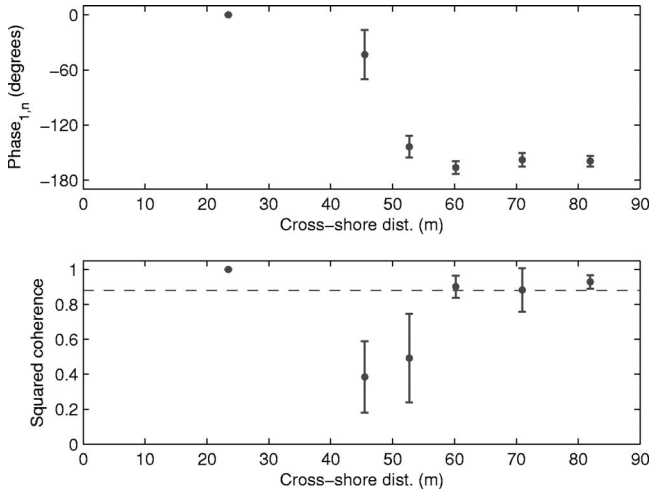

FIG. 4. (Top) relative phase between WG1 and other wave gages (n) for $f=0.0183$ Hz, (bottom) squared coherence between WG1 and other gages for $f=0.0183$ Hz, dashed line shows the 95% confidence level. Dots are mean of all six experimental runs, error bars represent ±one standard deviation, 6 dof.

between the offshore wave gage (WG1, $x=23.5$ m) and the other gages also confirms the nature of the motion. It is evident that WG1 is 180° out of phase with wave gages that are located on the opposite side of the nodal point ($x\geq 60$ m). The nodal point is apparent near $x=50$ m, where WG2 and WG3 are not coherent with WG1. We note that there is a somewhat linear variation of the relative phase in the region $45<x<55$ m, which is evidence that a small propagating component may exist at this frequency as well. However, at these locations the coherence is well below the 95% confidence level; hence, the phase estimates are poorly constrained. In summary, these results all indicate that the calculated seiching profiles, $\hat{\eta}$ and $\hat{u}$, associated with the lowest seiching mode provide a satisfactory representation of the dominant low-frequency motion during the experiments.

B. Observations and predictions of wave frequency oscillations

Next, we explore the relationship between the low-frequency standing waves and modulations in the absolute wave frequency. The absolute frequency $\omega(x,t)$ of the incident waves can be estimated by applying the Hilbert transform to the measured surface elevation time series.[29] The procedure involves first bandpass-filtering the time series about the incident wave frequency, in the present case we use a filter with a spectral width of 0.096 Hz (width $=48\Delta f$). Next, the Hilbert transform is applied to this filtered signal and used to calculate a time series of instantaneous phase. Taking the time derivative of this phase signal, using a simple forward-differencing scheme, results in a time series of instantaneous frequency.

The temporal mean, ω_0, of the resulting absolute frequency signal was calculated at all wave gages and for all experimental runs, and well matched the frequency of the wave paddle motion (i.e., the incident wave frequency at the offshore boundary). The maximum difference was 0.25% and, as expected, the temporal mean did not change spatially.

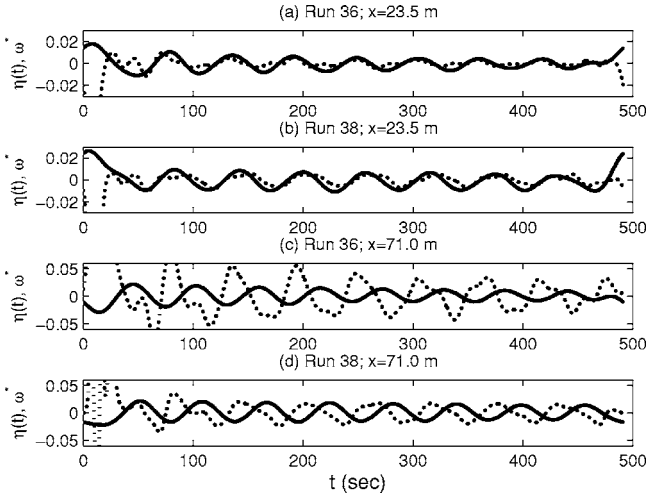

FIG. 5. Low passed surface elevation signal, η (solid), and demeaned absolute frequency, ω^* (dotted), observed at (a) WG1, run 36 (b) WG1, run 38 (c) WG5, run 36 and (d) WG5, run 38.

Representative time series of the demeaned frequency signal, $\omega^*(x,t)=\omega(x,t)-\omega_0$, measured at two of the wave gages for two separate wave conditions are shown in Fig. 5 along with the low-pass filtered ($f<0.03$ Hz) measured water surface signal η. These time series show clear oscillations in ω^* that appear well correlated with η, but with a phase shift. The amplitudes of the oscillations in wave frequency are on the order of 0.01–0.05 (rad/s) and are larger at the gage near the shoreline. The relative phase between ω^* and η also appears to vary in the cross-shore direction. This is most clearly evident in the time series from run 38 (compare the relative phase difference at $x=23.5$ m to $x=71.0$ m).

In order to quantify the variations in ω^* and their relationship to η, we define the amplitude A^* of the oscillations as $\sqrt{2}$ times the standard deviation of the ω^* time series and also calculate the observed phase differences between ω^* and η from the time lag of the maximum correlation between the two signals. The resulting amplitude and phase variations along the tank are compared to those produced by wave-current interaction theory in Figs. 6–9. The predicted values are obtained by solving Eq. (3) numerically using a standard forward-time, forward-space, finite difference scheme using a spatial step of 0.5 m and a time step of 0.1 s. The observed amplitudes of the dominant seiche mode, the previously calculated mode shapes ($\hat{\eta},\hat{u}$), and the frequency of the incident waves at the wavemaker are used to initiate the calculation, and 20 seiching cycles are simulated, resulting in a modeled time series of $\omega(x,t)$ at every cross-shore location. The numerical simulations demonstrate that the wave-current interaction theory predicts oscillations in ω at the observed seiching frequency, with some energy also existing at higher harmonics due to the nonlinear nature of the governing equation.

In a fashion similar to the experimental observations, the amplitudes of the predicted absolute frequency modulations are calculated as $\sqrt{2}$ times the standard deviation of the demeaned time series (ω^*) at each cross-shore position. In addition, using ten seiching cycles from the numerical simulations, the absolute phases of ω^*, η, and U are calculated (θ_ω, θ_η, and θ_U, respectively). These are then used to calculate the predicted relative phase at each cross-shore position.

Figures 6 and 7 show the predicted and observed cross-shore variation of A^* for the six experimental runs. The figures demonstrate that A^* increases in the direction of incident wave propagation for all cases and the maximum predicted A^* ranges from 3% to 5% of the mean incident wave frequency and this agrees very well with the observations. The predictions appear to perform somewhat better when the incident waves are of relatively higher frequency (Fig. 6). Further, both predictions and observations suggest that the maximum value of A^* varies from run to run, and relating the maximum value of A^* for each run to the maximum of $\hat{\eta}$ (shown in Fig. 3) strongly suggest that the maximum of A^* increases with increasing amplitude of the seich-

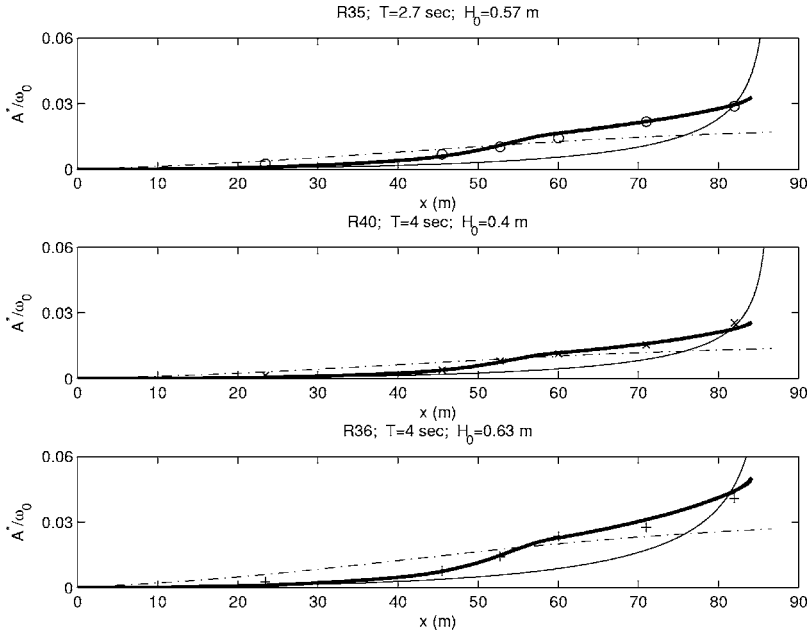

FIG. 6. Cross-shore variation of frequency modulation amplitude (normalized by the mean frequency) (a) run 35 (b) run 40 (c) run 36; shown are data (symbols), full model solution using Eq. (3) (thick solid line), asymptotic solution using Eq. (20) (dashed line), solution for constant depth basin Eq. (23) (dot-dashed line), and solution for plane beach basin Eq. (26) (thin solid line). The asymptotic solution (dashed line) often coincides with the full solution (thick solid line).

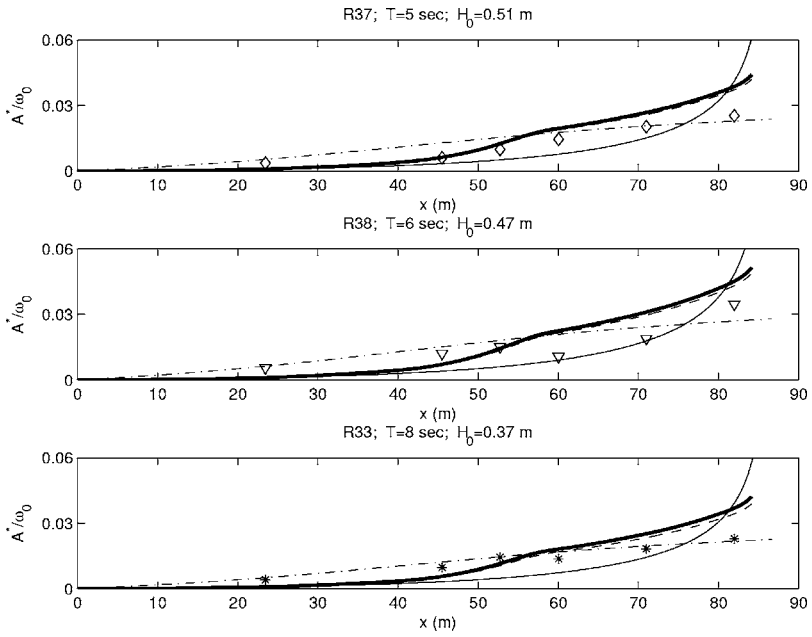

FIG. 7. Cross-shore variation of frequency modulation amplitude (normalized by the mean frequency) (a) run 37 (b) run 38 (c) run 33; shown are data (symbols), full model solution using Eq. (3) (thick solid line), asymptotic solution using Eq. (20) (dashed line), solution for constant depth basin Eq. (23) (dot-dashed line), and solution for plane beach basin Eq. (26) (thin solid line). The asymptotic solution (dashed line) often coincides with the full solution (thick solid line).

ing signal. We will examine the dependence of A^* on the seiching magnitude further in the next section.

The predicted and observed phase differences, $\theta_{\omega\eta}$, between ω^* and η are shown as a function of cross-shore location in Figs. 8 and 9. At the offshore boundary ω^* leads η by 90°, but the phase difference decreases steadily towards the shore. However, there is a 180° phase jump near $x=50$ m. This is a result of the 180° phase shift in η that occurs across the seiching nodal point. The predicted relative phases agree well with observations except at gages near the nodal point of the surface elevation where the data do not show a very abrupt phase jump. This is very likely a result of the fact that the measured η-signal is dominated by a small propagating component near the nodal point where the standing wave component is naturally zero. We note here that the predicted phase relationship between ω^* and U starts out at 180° at the wavemaker and decreases to 0° at the shoreline. Finally, the cross-shore variation of the phase difference is very similar for every run; hence, the phase relationships do not appear to be sensitive to the incident wave conditions. We elaborate on this observation further in the next section.

IV. DISCUSSION

A. Asymptotic behavior for a weak current

In this section we pursue analytical solutions to Eq. (1) in order to generalize the behavior of the absolute frequency modulations. For this purpose, we first nondimensionalize Eqs. (1) and (3) and identify a small parameter. A perturbation analysis then enables us to arrive at analytical expressions for the amplitude and phase of the frequency modulations.

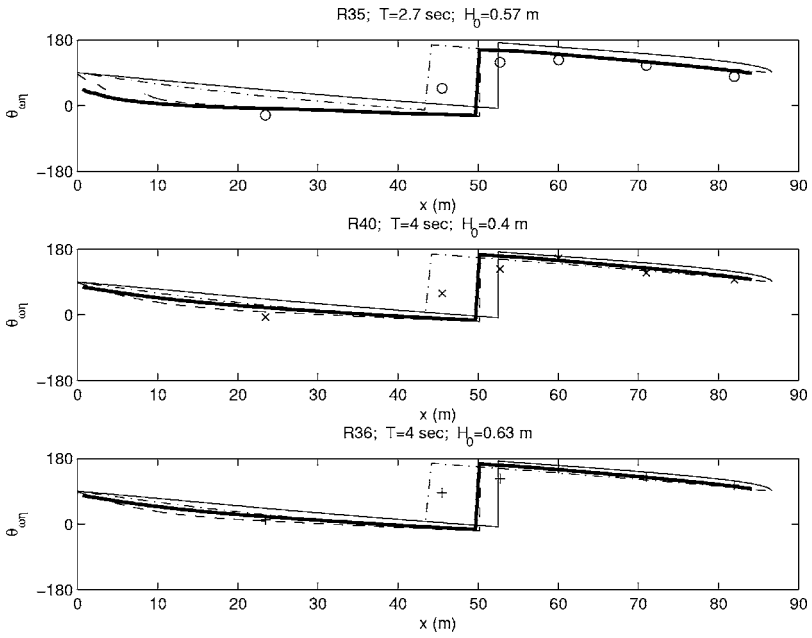

FIG. 8. Cross-shore variation of relative phase between frequency modulations and the low-frequency surface signal (a) run 35 (b) run 40 (c) run 36; shown are data (symbols), full model solution using Eq. (3) (thick solid line), asymptotic solution using Eq. (20) (dashed line), solution for constant depth basin Eq. (23) (dot-dashed line), and solution for plane beach basin Eq. (26) (thin solid line). The asymptotic solution (dashed line) often coincides with the full solution (thick solid line).

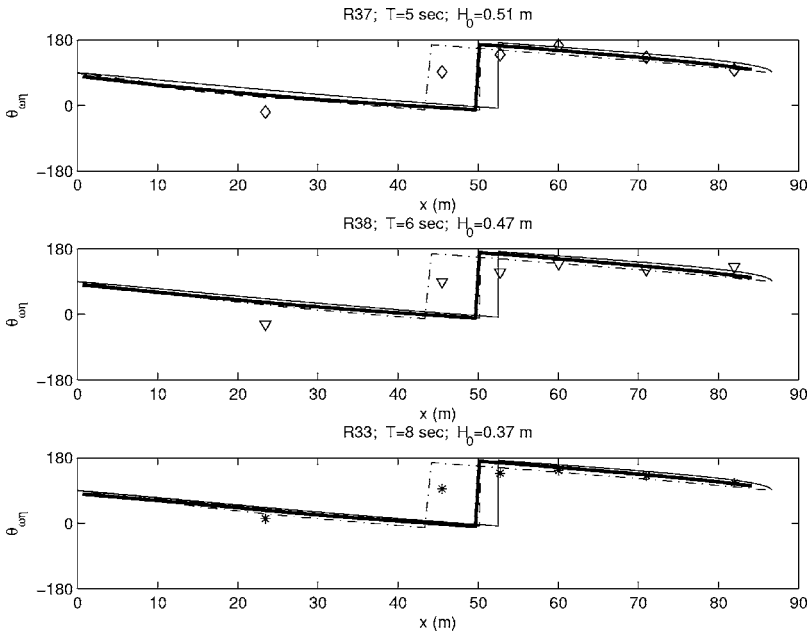

FIG. 9. Cross-shore variation of relative phase between frequency modulations and the low-frequency surface signal (a) run 37 (b) run 38 (c) run 33; shown are data (symbols), full model solution using Eq. (3) (thick solid line), asymptotic solution using Eq. (20) (dashed line), solution for constant depth basin Eq. (23) (dot-dashed line), and solution for plane beach basin Eq. (26) (thin solid line). The asymptotic solution (dashed line) often coincides with the full solution (thick solid line).

1. Nondimensional equations

Denoting nondimensional variables with primes and using subscript w and c to indicate scales associated with the incident progressive waves and the low-frequency currents, respectively, we have

$$\omega' = \frac{\omega}{\omega_w} \quad k' = \frac{k}{k_w}, \quad \text{where } \omega_w = \frac{2\pi}{T_w}, \quad k_w = \frac{\omega_w}{c_w}, \tag{6}$$

where T_w and c_w are the time and phase speed scales associated with the incident waves. Since we expect variations of the kinematic quantities to occur over the scales of the low-frequency current field, the independent variables x and t are nondimensionalized as

$$t' = \omega_c t \quad x' = k_c x, \quad \text{where } \omega_c = \frac{2\pi}{T_c} \quad k_c = \frac{\omega_c}{c_c}, \tag{7}$$

and T_c and c_c are the time and phase speed scales of the current.

We nondimensionalize the remaining variables as follows:

$$U' = \frac{U}{U_c}, \quad c'_{\mathrm{gr}} = \frac{c_{\mathrm{gr}}}{c_w}, \quad \eta' = \frac{\eta}{\eta_c},$$
$$q' = \frac{q}{q_w}, \quad p' = \frac{p}{p_w}, \quad h' = \frac{h}{h_m}. \tag{8}$$

Here, U_c and η_c are the velocity and amplitude scales associated with the low-frequency current field. The water depth scale, h_m, is chosen as the spatial average of the bathymetry. For the incident gravity waves we choose shallow water scales such that

$$c_w = \sqrt{g h_m}, \quad q_w = \frac{\omega_w}{h_m}, \quad p_w = \left(\frac{\omega_w}{h_m}\right)\left(\frac{U_c}{c_w}\right). \tag{9}$$

We now assume that $(\omega_c/\omega_w) \sim (k_c/k_w)$ and define a small parameter

$$\varepsilon = \frac{U_c}{c_w} \sim \frac{\eta_c}{h_m}.$$

Hence, we are assuming that the magnitude of the current is small compared to the incident wave speed (weak current) and the surface variations associated with the current field are small compared to the local water depth (small amplitude seiching). In these experiments the maximum values of $\hat{u}/c_w$ are estimated to be ~0.03 and the measured values of $\hat{\eta}/h$ at the shoreward gage (WG6) were ~0.05, as shown in Table I. This indicates a regime where the effects of wave-current interaction on the dispersion characteristics of the incident waves are weak. We note here, however, that it is possible that other dispersion effects that we have neglected (such as amplitude dispersion due to wave nonlinearities) may be of similar importance as wave-current interaction. However, our focus here is to identify and analyze the effects of current dispersion only, and in fact the model-data agreement in Figs. 6–9 suggests that current dispersion can explain most of the observed changes in absolute frequency.

2. Perturbation expansion

The resulting nondimensional governing equation is given by

$$\frac{\partial \omega'}{\partial t'} + (\varepsilon U' + c'_{\mathrm{gr}})\frac{\partial \omega'}{\partial x'} = \varepsilon k' \frac{\partial U'}{\partial t'} + \varepsilon q' \frac{\partial \eta'}{\partial t'} + \varepsilon^2 p' \frac{\partial \eta'}{\partial t'}. \tag{10}$$

Assuming that $\varepsilon \ll 1$, we can introduce a perturbation expansion such that $f' = f'_0 + \varepsilon f'_1 + O(\varepsilon^2)$, where f' represents one of the variables ω', k', c'_{gr}, q', and p'. It should be noted that all zeroth order quantities are allowed to vary in space (but not time) except for ω'_0, the mean wave frequency.

Hence, substituting and collecting terms at O(1) gives,

$$\frac{\partial \omega_0'}{\partial t'} + c'_{\mathrm{gr}_0}\frac{\partial \omega_0'}{\partial x'} = 0, \tag{11}$$

which is then naturally satisfied, and at $O(\varepsilon)$, we have

$$\frac{\partial \omega_1'}{\partial t'} + c'_{\mathrm{gr}_0}\frac{\partial \omega_1'}{\partial x'} = k_0'\frac{\partial U'}{\partial t'} + q_0'\frac{\partial \eta'}{\partial t'}, \tag{12}$$

where the coefficients c'_{gr_0}, k_0', and q_0' still need to be determined.

The zeroth order wavenumber k_0' can be deduced from the nondimensionalized dispersion relation

$$(\omega' - \varepsilon k' U')^2 = k'\frac{\tanh(k_w h_m k'(h' + \varepsilon\eta'))}{k_w h_m}. \tag{13}$$

Introducing the perturbation expansion to this equation and collecting terms of $O(1)$, we find

$$\omega_0'^2 = k_0' r_0', \quad \text{where } r_0' = \frac{\tanh(\mu k_0' h')}{\mu}, \tag{14}$$

where we have defined a parameter $\mu = k_w h_m$, which is indicative of the dispersiveness of the incident waves. Since we have used a shallow water scaling, we require that the waves are at most weakly dispersive; hence, $\mu < 1$ but is allowed to be nonzero. Next, we expand r_0' in μ, retaining terms up to $O(\mu^4)$, resulting in

$$r_0' = (k_0' h') - \tfrac{1}{3}\mu^2 (k_0' h')^3 + \tfrac{2}{15}\mu^4 (k_0' h')^5 + O(\mu^6). \tag{15}$$

Substitution of Eq. (15) into the $O(1)$ dispersion relation (14) results in a third-order polynomial in $k_0'^2$ that can readily be solved for k_0'.

A similar treatment of the other coefficients in Eq. (12) results in

$$c'_{\mathrm{gr}_0} = \frac{1}{2}\left(1 + \frac{1}{m_0'}\right)\frac{\omega_0'}{k_0'}, \quad \text{and } q_0' = \frac{\omega_0'}{2h' m_0'}, \tag{16}$$

where $m_0' = 1 + \frac{2}{3}\mu^2 (k_0' h')^2 + \frac{2}{15}\mu^4 (k_0' h')^4$. We now redimensionalize the $O(\varepsilon)$ governing equation (12) and obtain

$$\frac{\partial \omega_1}{\partial t} + c_{\mathrm{gr}_0}\frac{\partial \omega_1}{\partial x} = k_0\frac{\partial u}{\partial t} + q_0\frac{\partial \eta}{\partial t}. \tag{17}$$

We focus our attention on the case of a periodic current field and associated surface elevation as defined in Eq. (5). Writing $\omega_1 = A(x)\exp\{i\Omega t\}$, the governing equation (17) collapses into the form

$$\frac{dA}{dx} + P_A(x)A = Q_A(x), \tag{18}$$

where

$$P_A(x) = \frac{i\Omega}{c_{\mathrm{gr}_0}}, \quad Q_A(x) = \frac{i\Omega}{c_{\mathrm{gr}_0}}(k_0\hat{u} + q_0\hat{\eta}). \tag{19}$$

At the offshore boundary, we expect no frequency modulation; hence, we impose $A = 0$ at $x = 0$. The solution for the amplitude of the absolute frequency modulation $A(x)$ can then be written in closed form as

$$A(x) = R_A(x)\int_0^x \frac{Q_A(\xi)}{R_A(\xi)}d\xi, \quad \text{where } R_A(x) = e^{-\int_0^x P_A(\xi)d\xi}. \tag{20}$$

Given any arbitrary bathymetry profile $h(x)$ along with the associated seiching frequency Ω and seiching profiles $\hat{u}(x)$ and $\hat{\eta}(x)$, the functions $P_A(x)$, $Q_A(x)$ can be evaluated in a straightforward manner, and the integrals in Eq. (20) can be evaluated either analytically or numerically. This asymptotic solution is included in the data-model comparisons shown in Figs. 6–9. For most cases this asymptotic solution is visually indistinguishable from the full solution of Eq. (3). Slight deviations can be observed for the cases involving shorter incident wave periods, especially in the phase comparisons. Nonetheless, it is evident that the asymptotic solution captures the essential behavior of the kinematics.

B. Solutions for simplified basin configurations

The simplified form of the asymptotic solution allows us to better elucidate the general behavior of the wave-current interaction model. For example, it is instructive to analyze the simpler cases of a constant depth or plane sloping bathymetry for an enclosed basin. For these cases, analytic solutions are possible.

For an enclosed basin with uniform water depth, h, and length L, the first seiching mode is a simple cosine

$$\hat{\eta} = i\frac{H}{2}\cos\frac{\pi x}{L}, \quad \hat{u} = \frac{H}{2}\sqrt{\frac{g}{h}}\sin\frac{\pi x}{L}, \tag{21}$$

where H is twice the surface elevation amplitude of the seiching at the shoreline. The associated seiching period is given by

$$\frac{\Omega}{\sqrt{gh}} = \frac{\pi}{L}, \quad \text{or } T_c = \frac{2L}{\sqrt{gh}}. \tag{22}$$

Using the basin length L and mean water depth h_m associated with the experiments discussed here, we obtain a seiching frequency of 0.0232 Hz.

Substituting Eq. (21) into Eq. (20) and assuming that the incident waves are in shallow water (hence, $\mu = 0$), we find after some algebra that the amplitude of the frequency modulation for a constant depth basin is given by

$$A(x) = \frac{1}{8}\omega_0\frac{H}{h}\left\{\left(\sin\frac{\pi x}{L} - \frac{3\pi x}{L}\cos\frac{\pi x}{L}\right) + i\left(\frac{3\pi x}{L}\sin\frac{\pi x}{L}\right)\right\}. \tag{23}$$

Similarly, for a basin of length L containing a plane beach such that $h = h_c\left(1 - \frac{x}{L}\right)$, the first seiching mode is given by

$$\hat{\eta} = -i\frac{H}{2}J_0(2C\xi), \quad \hat{u} = \frac{H}{2}\sqrt{\frac{g}{h}}J_1(2C\xi),$$

where

$$\text{where } \xi = \sqrt{1 - \frac{x}{L}}, \tag{24}$$

and x points onshore, and J_0 and J_1 are Bessel functions of the zeroth and first order. The associated seiching period is given by

$$\frac{\Omega}{\sqrt{gh}} = \frac{C}{L} = \frac{1.916}{L}, \quad \text{or } T_c = \frac{\pi}{C}\frac{2L}{\sqrt{gh}} = 1.64\frac{2L}{\sqrt{gh}}. \tag{25}$$

Using $h_c = 2h_m$, we obtain a seiching frequency of 0.0201 Hz.

Using Eq. (20) in this case, we can obtain the shallow water solution

$$A(x) = \frac{1}{2}C\omega_0\frac{H}{h_m}\{[\cos(2C\xi)I_2(\xi) + \sin(2C\xi)I_1(\xi)] + i[\cos(2C\xi)I_1(\xi) - \sin(2C\xi)I_2(\xi)]\}, \tag{26}$$

where $I_1(\xi)$ and $I_2(\xi)$ are integrals involving trigonometric and Bessel functions given by

$$I_1(\xi) = \int_1^{\xi}\left\{\cos(2C\zeta)J_1(2C\zeta) - \frac{1}{2}\sin(2C\zeta)J_0(2C\zeta)\right\}\frac{1}{\zeta^2}d\zeta, \tag{27}$$

$$I_2(\xi) = \int_1^{\xi} -\left\{\sin(2C\zeta)J_1(2C\zeta) - \frac{1}{2}\cos(2C\zeta)J_0(2C\zeta)\right\}\frac{1}{\zeta^2}d\zeta. \tag{28}$$

The magnitude of the frequency modulation for these cases can be deduced using

$$|A(x)| = \sqrt{(\mathrm{Re}\{A(x)\})^2 + (\mathrm{Im}\{A(x)\})^2}. \tag{29}$$

In both cases, this can be written as

$$|A(x)| = \omega_0\frac{H}{h_m}F(x), \tag{30}$$

where $F(x)$ is a monotonically increasing function with distance from the wavemaker x. The absolute magnitude of the frequency modulation increases with incident wave frequency ω_0; however, the relative magnitude $|A|/\omega_0$ is only a function of the ratio between the seiching height and the water depth (H/h_m) and normalized cross-shore distance (x/L). The maximum value of the frequency modulation occurs at the shoreline $x=L$. For the constant depth basin the maximum value is

$$|A| = \frac{3\pi}{8}\omega_0\frac{H}{h_m}.$$

Note that for a 10% frequency modulation to be observed, the ratio of H/h_m need only be ≈ 0.085. For the plane beach solution the magnitude of the frequency modulation tends to infinity in the limit as x approaches L.

The relative phase with respect to the U-velocities, $\theta_{\omega U}$, is contained in the complex amplitude $A(x)$ and is given by

$$\theta_{\omega U} = \arctan\left\{\frac{\mathrm{Im}\{A(x)\}}{\mathrm{Re}\{A(x)\}}\right\}. \tag{31}$$

The relative phase between ω and η can be obtained by subtracting the phase between η and U, which is 90° seaward of the nodal point in η and −90° shoreward of it. For both example cases $\theta_{\omega U}$ tends to 180° at the wavemaker ($x=0$) and decreases monotonically to zero at $x=L$, consistent with the experimental observations. Also of note is that the cross-shore variation of $\theta_{\omega U}$ is independent of the initial incident wave frequency ω_0, the seiching height H or the mean water depth h_m. The exact shape of the phase progression depends only on the seiching profiles $\hat{u}(x)$ and $\hat{\eta}(x)$, which in turn depend on the cross-shore variation of $h(x)$.

We note here that these example cases exhibit many of the same characteristics as more complicated scenarios. In particular, in the shallow water limit, it can be shown analytically for any arbitrary depth profile $h(x)$ that the relative magnitude $|A|/\omega_0$ is only a function of (H/h_m) and (x/L). In other words, in the shallow water limit the quantity $|A|/(\omega_0 H)$ should exhibit the same cross-shore profile regardless of the incident wave conditions. Although our experiments also include some intermediate depth conditions, we nonetheless find that the graphs of $|A|/(\omega_0 H)$ versus cross-shore position predicted by the full theory for each wave condition essentially collapse into a single line, as shown in the top panel of Fig. 10. We note that all experimental runs reside in the narrow range between run 40 and run 33, with the exception being the run with the smallest wave period (run 35, $T=2.7$ s, solid line). Examining Fig. 10, we can conclude that the magnitude of the absolute frequency modulation increases with the mean frequency. It can also be shown analytically that the phase between ω^* and U starts out at 180° and decreases to 0° for a plane beach as well. Numerical solutions of the full governing equations for our experimental conditions (see Fig. 10, bottom panel) suggest that this is also a generally valid result.

Finally, we address if the constant depth or plane beach solutions can provide a useful approximation for the situation involving the actual bathymetry. For this purpose, solutions for these example cases are included in the comparisons of frequency modulation amplitude and phase in Figs. 6–9. We find that the approximate solutions provide the correct order of magnitude estimate for the modulation magnitude and phase, although details related to the location of the phase jump are inaccurate, because the zero-crossing associated with the seiching profiles vary somewhat from one bathymetry to another.

C. Wave height response to low frequency seiching motions

In addition to the wave frequency effects, in the presence of time-varying currents we expect that wave heights will also be modulated due to current-induced shoaling. For the present case of an oscillating current field and total water depth, with spatially varying amplitudes, we can analyze the characteristics of the expected wave height variations using the wave action balance equation,

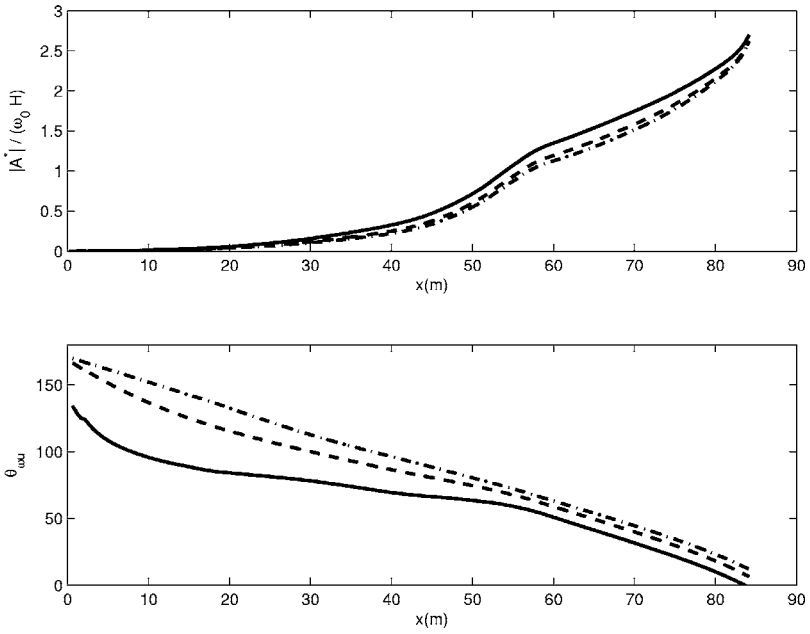

FIG. 10. Cross-shore variation of (top panel) normalized magnitude $|A^*|/(\omega_0 H)$, and relative phase (bottom panel) between the frequency modulation and the low-frequency current for run 35 (solid), run 40 (dashed), and run 33 (dot-dashed).

$$\frac{\partial}{\partial t}\left\{\frac{E}{\sigma}\right\} + \frac{\partial}{\partial x}\left\{(U + c_{\mathrm{gr}})\frac{E}{\sigma}\right\} = \frac{D}{\sigma}, \tag{32}$$

where E is the wave energy and σ is the relative frequency and is equal to $(\omega - kU)$ (Ref. 10, p. 97). The presence of a surf zone and associated wave dissipation, D, due to wave breaking adds considerable complication to the problem. Specifically, significant uncertainty still exists regarding the effect of wave breaking on a wave train with a spatially and temporally varying height.[30] In light of such uncertainty, we limit our attention to the region outside the surf zone.

We solve Eq. (32) (with $D=0$) numerically along with the governing Eq. (3). We define the fluctuating component $E^*(x,t) = E(x,t) - E_0(x)$ [where $E_0(x)$ is the temporal mean wave energy computed at each cross-shore position] and compute its amplitude B^* as was done for the absolute frequency modulations. Results of the cross-shore variation of $(|B^*|/E_0)$ for run 37 are shown in Fig. 11. We determine an approximate break point location from the observations and depict the results for the region inside the surf zone with an altered line type to indicate that the results are not reliable there, since wave breaking is neglected in the calculation. Figure 11 indicates that the magnitude of the wave energy fluctuation outside the surf zone increases with distance from the offshore boundary and reaches approximately 5% of the mean wave energy near the breaker line. For the experimental conditions this corresponds to a wave height modulation of about 1.4 cm offshore of the surf zone. Unfortunately, for the present data set there was only a single wave gage (WG1) offshore of the breaker line. At that location ($x = 23.5$ m) the predicted wave height modulation amplitude is

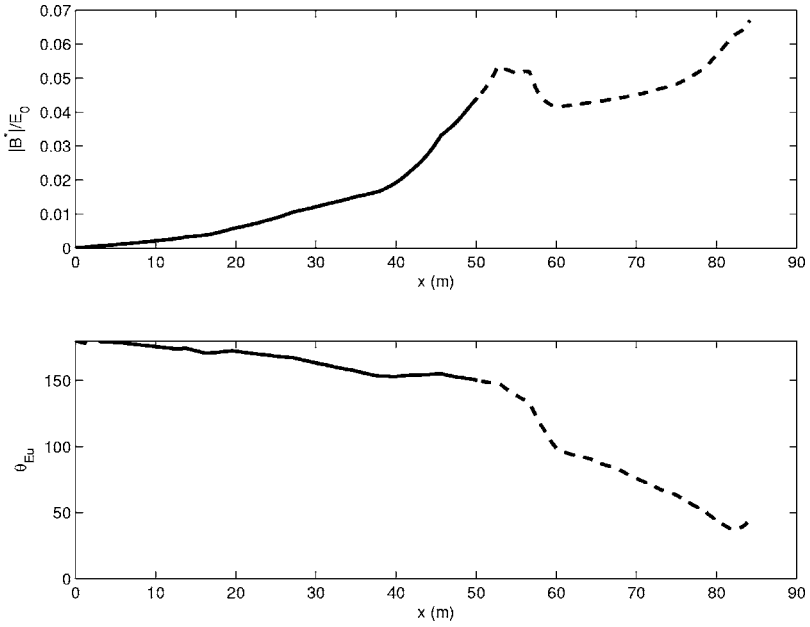

FIG. 11. Cross-shore variation of the magnitude B^* (top) and phase (bottom) of the predicted wave height modulation for run 37.

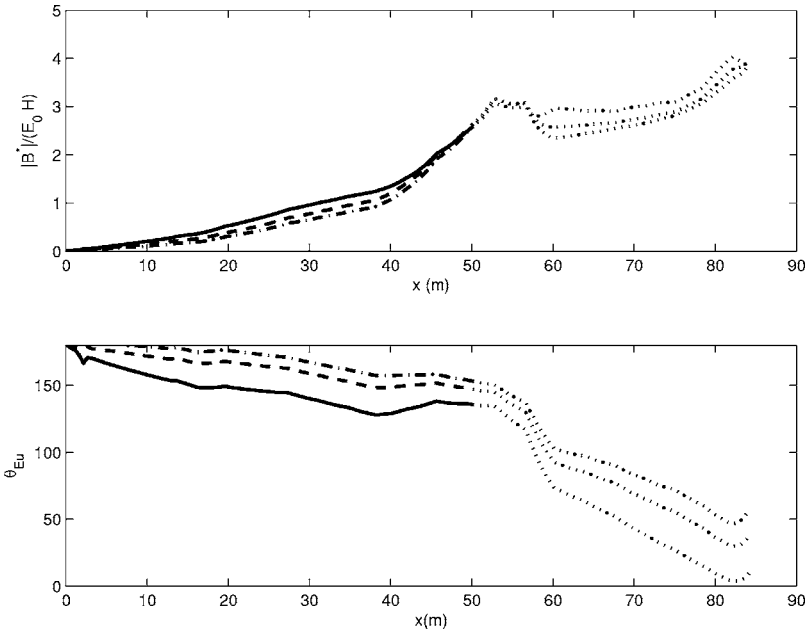

FIG. 12. Cross-shore variation of (top panel) normalized magnitude $|B^*|/(\omega_0 \hat{\eta}_{\max})$ and relative phase (bottom panel) between the energy modulation and the low-frequency current for run 35 (solid), run 40 (dashed), and run 33 (dot-dashed).

only ~4 mm for the tested wave conditions. These small signals could not be reliably extracted from the wave gage records due to typical sensor noise levels.

Despite our inability to confirm these results observationally, it may be of interest for future studies to explore the theoretical behavior of the wave energy modulation. For this purpose, we carry out a perturbation analysis for the wave energy equation (32). We follow a procedure that parallels the treatment of the frequency modulations in Sec. IV A; hence we nondimensionalize Eq. (32), define $E'(x,t) = E'_0(x) + \varepsilon E'_1(x,t)$, redimensionalize the resulting $O(\varepsilon)$ equation and define

$$E_1 = B(x)\exp\{i\Omega t\} \tag{33}$$

arriving at an ordinary differential equation of the form (18) for $B(x)$. For a constant depth basin in the shallow water limit, we find the analytical solution

$$B(x) = \frac{1}{2}E_0\frac{H}{h}\left\{-2\sin\frac{\pi x}{L} - \frac{5\pi x}{2L}\cos\frac{\pi x}{L} + i\frac{5\pi x}{2L}\sin\frac{\pi x}{L}\right\}. \tag{34}$$

Hence, we expect that the magnitude of the wave energy modulation is proportional to the incident wave energy $E_0(x)$ and the ratio (H/h). Of note is that the wave energy modulation in the shallow water limit is independent of wave frequency. Analysis of solutions to the full governing Eqs. (32) for all six cases (Fig. 12) indicate that this is a generally valid result. Again, all runs reside in the narrow range between run 40 and run 33, with the only exception being the high-frequency case, run 35. This indicates that dispersive effects (i.e., nonzero μ) tend to increase the modulation amplitude. The phase variation between E_1 and the current velocity U tends to 180° at the wavemaker and decreases towards shore and is, once again, primarily a function of (x/L) with dispersive effects decreasing the phase difference.

In the presence of wave breaking, we do not consider wave height modulations to be as clear of an indicator of wave-current interaction with unsteady currents as observations of frequency modulations. This is primarily because induced wave height modulations will be modified by the breaking process, and perhaps entirely destroyed in shallow water areas. In contrast, the frequency modulations remain and gain magnitude towards shore. Further, we expect that temporal wave height modulations can be generated due to a number of other processes unrelated to wave-current interaction (e.g., partial wave reflection from the beach). In addition, processes that cause a modulation in the incident wave frequency are scarce, yet small variations in frequency can be observed reliably using the Hilbert transform method used herein. Hence, we consider that analysis of the wave frequency enables us to pinpoint in detail effects of time-varying currents on incident waves.

V. CONCLUSIONS

The effects of unsteady currents and water depths on the kinematics of surface gravity waves were analyzed using a data set from a large scale laboratory experiment. Wave-current interaction theory predicts that unsteady currents and water depths modulate the absolute wave frequency spatially and temporally. For the case of a periodic current field in a nearshore domain, predictions of the frequency modulation amplitude and phase were compared with observations. We found that the cross-shore variation of the magnitude and phase of the frequency modulation are well predicted by the theory.

Wave-current interaction theory predicts (and observations confirm) that the magnitude of the frequency modulation increases with distance towards shore, and can reach ~5% of the mean wave frequency. The theory also predicts the modulation magnitude to be directly proportional to the amplitude of the low-frequency current for shallow or intermediate water waves, and that increasing the relative water depth of the incident waves somewhat amplifies the frequency modulation response. For the specific situation of

incident waves interacting with seiching motions, we find that the consideration of an equivalent constant depth or plane beach case provides a simple means of assessing the order of magnitude of the frequency modulation effect.

The dependence of the modulations on the amplitude of the unsteady current should best be viewed as an indicator of the importance of the time rate of change of both the currents ($\partial u/\partial t$) and the water depth ($\partial \eta/\partial t$). In the present case, the time scale of the oscillating current field is the same for all the tested conditions (i.e., the seiching period remains constant); hence, variations in current accelerations are directly related to variations in seiching amplitude from run to run. In these data, the current accelerations are approximately $u_{\max}/T=5$ cm/55 s$\approx$0.1 cm/s^2 and the surface rate of change is $H/T=3$ cm/55 s$\approx$0.05 cm/s. For comparison, a realistic scale for cross-shore standing waves in the surf zone (surf beat), is $H/T=10$ cm/100 s$\approx$0.1 cm/s. This indicates that modulations in the absolute frequency, to date unexplored, may not be uncommon in the nearshore, especially in areas with energetic low-frequency wave fields.

Data specifically applicable to the effects of unsteady currents are rare; hence, the data set analyzed herein is unique. For example, in a natural situation, observed wave frequency variations are commonly due to the typical temporal variability of the incident wave field or changes in the local winds. Such variations are completely independent from wave-current interaction effects, but may be difficult to distinguish in field data. In contrast, the present data set has allowed us to examine the wave-current interaction effect in isolation and provides a detailed verification of theoretical predictions.

ACKNOWLEDGMENTS

We thank Patricio Catalán, Dan Cox, Joe Long, Tim Maddux, Chris Scott, and the staff at the O. H. Hinsdale Wave Research Lab (HWRL) for their efforts in conducting the experiments. Portions of this work were funded by The National Science Foundation under Grant Nos. OCE-0351153 and EEC-0244205. We would also like to thank Jim Kirby and an anonymous reviewer for helpful comments. This paper is dedicated to the memory of Retired Rear Admiral I. Turgut Özkan.

[1] P. J. Unna, "Waves on tidal streams," Nature (London) **149**, 219 (1942).
[2] A. J. Battjes, "A case study of wave height variations due to currents in a tidal entrance," Coastal Eng. **6**, 47 (1982).
[3] F. I. Gonzalez, "A case study of wave-current-bathymetry interactions at the Columbia River entrance," J. Phys. Oceanogr. **14**, 1065 (1984).
[4] J. Yu, "On the instability leading to rip currents due to wave-current interaction," J. Fluid Mech. **549**, 403 (2006).
[5] H. T. Özkan-Haller and Y. Li, "Effects of wave-current interaction on shear instabilities of longshore currents," J. Geophys. Res. **108**, 3139, DOI: 10.1029/2001JC001287 (2003).
[6] S. M. Henderson, R. T. Guza, S. Elgar, and T. H. C. Herbers, "Refraction of surface gravity waves by shear waves," J. Phys. Oceanogr. **36**, 629 (2006).
[7] M. S. Longuet-Higgins and R. W. Stewart, "Changes in the form of short gravity waves on long waves and tidal currents," J. Fluid Mech. **8**, 565 (1960).
[8] M. S. Longuet-Higgins and R. W. Stewart, "The changes in amplitude of short gravity waves on steady nonuniform currents," J. Fluid Mech. **10**, 529 (1961).
[9] D. H. Peregrine, "Interaction of water waves and currents," Adv. Appl. Mech. **16**, 9 (1976).
[10] C. C. Mei, *The Applied Dynamics of Ocean Surface Waves* (World Scientific, Singapore, 1983), p. 740.
[11] I. G. Jonsson, "Wave current interactions," *The Sea Volume 9: Ocean Engineering Science*, edited by B. LeMehaute and D. M. Hanes (Wiley, New York, 1990).
[12] G. P Thomas and G. Klopman, "Wave-current interactions in the nearshore region," J. Fluid Mech. **6**, 257 (1997).
[13] G. L. Mellor, "The three dimensional current and surface wave equations," J. Phys. Oceanogr. **35**, 2291 (2005).
[14] P. J. Unna, "White horses," Nature (London) **148**, 226 (1941).
[15] N. F Barber, "Behaviour of waves on tidal streams," Proc. R. Soc. London, Ser. A **198**, 81 (1949).
[16] D. E. Irvine, "The kinematics of short wave modulation by long waves," *The Ocean Surface*, edited by Y. Toba and H. Mitsuyasu (Reidel, New York, 1985), pp. 129–134.
[17] H. L. Tolman, "The influence of unsteady depths and currents of tides on wind-wave propagation in shelf seas," J. Phys. Oceanogr. **20**, 1166 (1990).
[18] H. L Tolman, "Effects of tides and storm surges on North Sea wind waves," J. Phys. Oceanogr. **21**, 766 (1991).
[19] J. Wolf and D. Prandle, "Some observations of wave-current interaction," Coastal Eng. **37**, 471 (1999).
[20] B. Jones, "A numerical study of wave refraction in shallow tidal waters," Estuarine Coastal Shelf Sci. **51**, 331 (2000).
[21] S. Elgar and R. T. Guza, "Shoaling gravity waves: Comparisons between field observations, linear theory, and a nonlinear model," J. Fluid Mech. **158**, 47 (1985).
[22] G. B. Whitham, *Linear and Nonlinear Waves* (Wiley, New York, 1974).
[23] M. W. Dingemans, *Water Wave Propagation Over Uneven Bottoms, Part 1-Linear Wave Propagation* (World Scientific, Singapore, 1997), p. 471.
[24] B. S. Wilson, *Encyclopedia of Oceanography*, edited by R. W. Fairbridge (Academic, New York, 1966).
[25] J. T. Kirby, H. T. Özkan-Haller, and M. C. Haller, "Seiching in a large wave flume," in *Proceedings of Coastal Engineering: 30th International Conference*, ASCE, San Diego, CA, pp. 1159–1171 (2006).
[26] P. A. Catalán, "Hybrid approach to estimating nearshore bathymetry using remote sensing," M.Oc.E. thesis, Oregon State University (2005).
[27] P. A. Catalán and M. C. Haller, "Remote sensing of breaking wave phase speeds with application to nonlinear depth inversions," Coastal Eng. **55**, 93 (2008).
[28] C. P Scott, D. T. Cox, T. B. Maddux, and J. W. Long, "Large-scale laboratory observations of turbulence on a fixed barred beach," Meas. Sci. Technol. **16**, 1903 (2005).
[29] W. K. Melville, "Wave modulation and breakdown," J. Fluid Mech. **128**, 489 (1983).
[30] J. Veeramony and I. A. Svendsen, "Wave breaking in wave groups," J. Waterway, Port, Coastal, Ocean Eng. **127**, 200 (2001).